# Wall-slip effects on the Yield-stress fluid flows in the rigid and deformable channel


**Ashish Garg**[1,2] *, **Pranjal Prasad**[3]

[1]Seminare Private Limited, Delhi, India

[2]Department of Chemical Engineering, Indian Institute of Technology Delhi, India

[3]Department of Mathematics and Statistics, University of Massachusetts Amherst, MA, USA



September 4, 2023



## Abstract

Yield stress fluids flow through deformable conduits and are prevalent in nature and have numerous technological applications [1, 2, 3, 4, 5, 6, 7, 8, 9, 10, 11]. In this paper, we focus on investigating the impact of many factors such as the deformability of the channel wall, yield stress, shear thinning, and shear thickening index in the presence of slip and compared it with flow dynamics with no-slips as predicted by Garg and Prasad [12]. Using lubrication theory, we have derived a model for the velocity profiles and flow rate using the Herschel–Bulkley rheological model in rigid and deformable shallow channels with slip-walls. To model deformable walls, we have utilized small displacement structural mechanics and perturbation theory presented by Gervais et al. [13] and Christov et al. [14], respectively. Notably, our newly developed model encompasses the flow characteristics of Newtonian fluids, power–law fluids, and Bingham fluids, both with and without wall-slip, as observed in previous literature [13, 14, 15, 16]. We find that the deformability increases the same effective channel height with and without wall-slip but the flow rate is increased more when slips are present within the channel. We find many scalings for the flow rate under different regimes of applied pressure and the deformability parameter. It is known that due to the presence of yield stress, a threshold inlet pressure is required for the onset of flow in the channels unlike in the case of the Newtonian or power–law fluids. Garg and Prasad [12] finds that below this threshold, the flow is choked in the channels with plug height the same as the channel height: we find the same observations in the presence of slips. Although in case of deformable channels an early onset of flow with the pressure is found in comparison to the rigid channel. We observe the back flow due to deformability in the channel when the yield surface is between $H_o/2 < H_p < (H_o + \delta)/2$, where $H_o$ represents the initial height of the channel without deformability. $H_p$ is the height of the yield surface. $\delta$ is the increase in



*Email: ashish.garg.iisc@gmail.com, ashish@seminare.in

channel's height due to the elastic walls. Beyond choked flow, the plug height starts to decrease for both the rigid and the deformable channels with the pressure. We also observe that for any given applied pressure and yield stress, the $(H_p)_{\text{deformable}} < (H_p)_{\text{rigid}}$. This suggests that deformable elastic walls decrease the plug region in comparison to the rigid channel. We also find that the wall-slip has no effect on the plug region and the onset of flow. In the presences of wall–slip, we also find that increasing the yield stress leads to a decrease in the velocity in the plug flow as well as in the non–plug flow regions. Increasing yield stress also leads to increasing the yield surface height and the solid plug in the central region due to which there is decrease in the flow rate similar to as found by Garg and Prasad [12]. Further, we also find that the shear thinning/thickening index does not affect the plug height, although as the index increases, the flow rate starts to decrease due to the corresponding increase in shear thickening of the material.

**Keywords:** Yield stress fluid flows, Wall-slips, Herschel–Bulkley fluids, deformable channels, lubrication approximation.

# 1 Introduction

Slip, or the relative motion between a fluid and a solid boundary, can have a significant effect on the flow behavior of yield-stress fluids in deformable channels [17, 18, 19]. Yield-stress fluids are materials that do not flow until a critical stress is applied, after which they begin to flow like a fluid. Examples include certain types of gels, pastes, and concentrated suspensions [4, 5, 6, 20, 21].

Yield stress fluids exhibit slip at the channel walls during flow. When these fluids flows through a channel, a thin layer close to the walls develops, where the fluid's velocity is different from the velocity of the wall [22, 23]. This slip behavior is common in yield stress fluids. The slip phenomenon occurs due to the interaction between the fluid molecules and the solid surfaces of the channel walls. At the wall, the fluid molecules experience different forces and interactions compared to the bulk of the fluid away from the wall [24, 25, 26]. As a result, the fluid molecules in the boundary layer near the wall can slip or slide along the surface. The presence of slip at the channel walls can affect the overall flow behavior of an yield stress fluid [17, 27, 28]. Slip reduces the effective shear rate at the wall, which, in turn, affects the effective viscosity of the fluid near the wall [28]. This means that the fluid behaves as if it has a lower viscosity than it would if no slip were present [29].

The extent of slip depends on various factors, including the nature of the fluid, yield stress magnitude, the channel's geometry, surface properties of the fluid, deformability, and the flow conditions [30, 31]. Slip can have significant implications for fluid dynamics, heat transfer, and mass transport in the channel [32]. The flow characteristics of yield-stress materials also highly depend on the flow geometry in which they flow [33], in particular, the features of the solid wall surfaces that they are in contact with. In this context, slippery characteristics causes the macro and micro scale drag reductions [34, 35, 36, 37], as well as fluid manipulations in microfluidic devices [38, 39]. The shape and dimensions of the deformable channel affects how slip impacts the flow behavior [40]. The interaction between slip and channel deformability can lead to complex flow behaviors. When slip occurs, it reduces the apparent viscosity of the yield-stress fluid near the wall [28]. This slip effect can be significant when the slip length is comparable to or larger than the channel dimensions [41, 42]. This is the reason that narrow channels may experience more significant slip effects than wider channels. Slip is pronounced at micro and nano scale and plays an important role in flow dynamics of yield stress flow such as blood flow in veins and arteries [43]. To reduce food and healthcare waste where yield stress materials tend to get stuck, smart materials employs a stick-slip mechanism [44, 45, 46]. The stick-slip mechanism involves alternating periods of static friction (stick) and dynamic motion (slip). In this context, it can be used to facilitate the controlled release of yield stress materials that tend to adhere to surfaces, like food and healthcare products [47]. Reducing the underwater adhesion of barnacles on ships is an effective way to minimize drag and improve fuel efficiency [48]. When barnacles attach to a ship's hull, they create rough surfaces that increase resistance in the water, resulting in higher fuel consumption and reduced vessel speed [49]. To address this issue, several strategies are employed: biocide paints, copper-based antifouling paints, foul-release coatings, bubble and air-curtain systems (Leidenfrost effect drag reduction) [50]. Most of these methods induces slip to the ship vessels [51, 52, 53, 54]. Effect of slips depends on the magnitude of the yield stress also. For example, in materials with a high yield stress, even a small amount of slip can significantly impact flow behavior [55, 56, 57]. In contrast, for materials with low yield stress, slip effects may be less pronounced. Even different flow regimes, whether laminar or turbulent, affect the influence of slip on yield-stress flows differently. Turbulent flows may disrupt the slip layer and lead to different flow characteristics compared to laminar flows [58, 59].

In order to model yield stress fluids, we use Herschel–Bulkley rheological model (described in following Section 3.2), which describes all the yield stress, the shear thinning, and shear thickening properties of the material. Herschel–Bulkley fluids flow in the deformable channels are common with several applications. Examples include in food processing [1, 2, 3], in the oil and gas industry [7], in the biomedical applications [8, 9] (flow through tubes, pipes, and hoses) for conveying, distribution, and transport in polymer processing industries, such as extrusion and injection molding [60, 61], in the pharmaceutical formulations and processing [62, 63, 64], in the waste management [65, 66, 67]. To optimize the processing conditions, preventing blockages, and ensuring consistent product quality, the understanding of the flow behavior of yield stress materials in the flexible channels play a vital role. As the flow behaviour for yield stress materials highly depends on the slips, the modelling of slip dynamics is essential for efficient handling and processing.

The methods devised to handle various non–Newtonian flows in deformable conduits face varied analytical challenges and therefore, require computations [68, 69, 70, 71]. The existing literature exhibits lack of advancements in most aspects of non–Newtonian flow in deformable conduits, leaving several research gaps where common problems remain unexplored. Several works have developed models for fluid flow in deformable conduits. The majority of these are on Newtonian fluids, although some have considered non–Newtonian rheologies. An example of the former is the widely adopted one–dimensional (1D) Navier–Stokes flow model, specifically applied to deformable tubes in various studies [72, 73, 74, 75]. This 1D model is limited in the sense that it is valid only for Newtonian flows with a large number of parameters, making it impractical for any practical applications. Sochi [76] studied the flow of Newtonian and power–law fluids in elastic tubes. However, both these models: the (1D) Navier–Stokes flow model and the model derived by Sochi [76] are not for the channel studies. Fusi et al. [77] gave a lubrication approximation method for solving Bingham plastic flows in symmetric long channels of non–constant width. This model lacked considering the effects of shear thinning and shear thickening properties of the fluid. Also, it did not account for the flexibility of the channel walls. Panaseti et al. [78] extended the method of Fusi et al. [77] to study Herschel–Bulkley fluids to include the shear thinning and shear thickening properties of the fluid with pressure–dependent consistency index and yield stress, and derived analytical solutions for channels with linearly varying width. But this investigation was only on rigid channel walls. Fusi and Farina [79] extended the lubrication-approximation method for axisymmetric viscoplastic flows in long tubes of varying radii assuming rigid walls of the tube. Housiadas et al. [80] used their method to solve the flow in a tube of constant radius of a Bingham plastic with yield stress and plastic viscosity varying linearly with pressure. Fusi et al. [81] adopted the method of Fusi and Farina [79] to study the flow of a Bingham plastic in tubes of varying radius, e.g. expanding or contracting tubes, or tubes with a stenosis. Howwever, this model focused solely on tubes. Also, it did not take into account the influence of fluid characteristics that lead to shear thinning and shear thickening. Vajravelu et al. [10] attempted to model the flow of Herschel–Bulkley fluids in elastic tubes as a representation of non–Newtonian behavior. Although they derived their model with a crude assumption that the ratio of the radius of tube to the radius of the yield surface is constant under deformable walls. In addition, it's worth noting that the study by Vajravelu et al. [10] did not incorporate or account for the influence of slips in their modeling. Also, their research, unlike our research, was conducted on tubes rather than channels (as in our case). Recently Garg and Prasad [12] conducted studies on the Herschel–Bulkley fluid flow in deformable channels, but without wall-slip effect. As evident from the above literature, that the slip effects are important in the yield stress fluid flow. In this paper, we investigate the flow of Herschel-Bulkley fluids in the rigid and deformable channels, taking into account the influence of wall-slip effects.

The deformability of a shallow channel is an important factor that impacts both the effective pressure drop across the channel and the resultant flow configuration [13, 14]. This happens because the flow rate is highly influenced by the size of the cross–sectional dimensions, showing a strong relationship to the fourth power [14]. Consequently, even a small perturbation in the geometry of the channel can result in substantial changes in the pressure drop and flow characteristics. Gervais et al. [13]'s model explains the alteration in flow rate caused by deformations, linking a Hookean elastic response with the lubrication approximation for the Stokes flow. However, the presence of a model parameter requiring empirical determination for each channel shape makes their model difficult to use. Through a perturbation technique for the flow Christov et al. [14] derived a relation to the parameter introduced by Gervais et al. [13] . In our study, we assume the small displacement structural mechanics from Gervais et al. [13] and the perturbation theory presented by Christov et al. [14]. Using these, we formulate a model for a deformable channel wall for the yield stress fluid flows with wall-slip effect. Also, using the lubrication assumption in shallow conduits (particularly, where the ratio of height to width and height to length are both considered small),the impact of channel flexibility on velocity profiles and the flow rate is also investigated. Further, the influence of fluid properties such as yield stress and shear thinning/thickening index along with varying pressure conditions are analyzed in the presence of wall-slip.

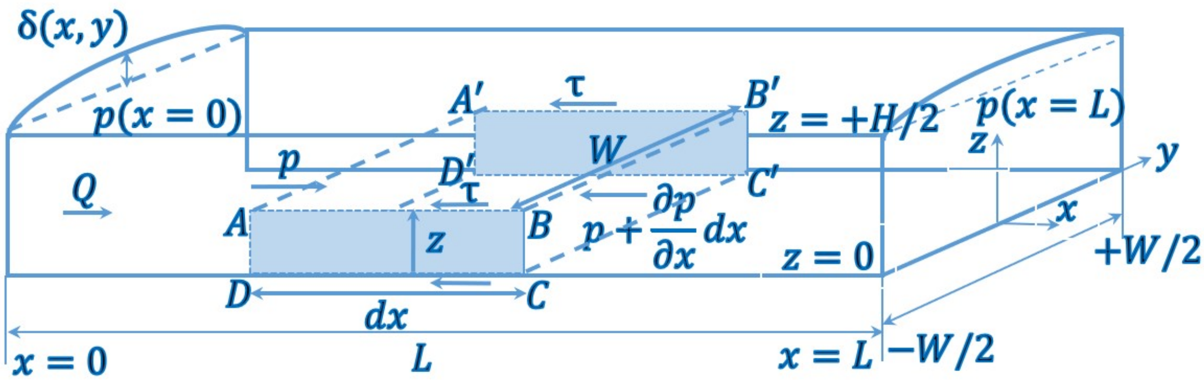


Figure 1: Schematic diagram of the upper half part of the shallow channel of length $L$, cross–sectional width $W$, and height $H$. The Cartesian axis is taken at the mid plane of the channel.

We consider a shallow rectangular channel characterized by dimensions: length $L$, width $W$, and height $H$, satisfying the conditions $H \ll W$ and $H \ll L$, as depicted in Figure 1. The upper surface of this channel is comprised of an elastic sheet securely attached along the edges of the vertical channel wall enabling it to undergo deformation. A pressure difference prompts a flow rate $Q$ in the $x$ direction. The flow's normal stresses acting on the walls cause the flexible upper wall of the channel to deform upwards in the positive $z$ direction, away from the $x - y$ plane.

This deformation shapes the constant configuration of the channel's top surface, represented as $z = H(x, y) = H_o + \delta(x, y)$, where $\delta(x, y)$ symbolizes the vertical deformation, as illustrated in Figure 1. At $x = 0$, a pressure field $p(x)$ is introduced at the reservoir, while the exit pressure is considered zero for reference. Presently, we abstain from assuming any specific magnitude for the displacement. However, under small displacement of the deformable walls, we anticipate that, the magnitude $|\delta|$ remains significantly smaller than $W$ within our context.

The structure of the paper is outlined as follows. Section 2 describes the governing equations, while the Section 3 presents the model's derivation. In the Section 4, we present and analyze the results. This includes the investigation of the impact of slips with and without yield stress fluid flows on the necessary applied pressure required to induce flow. We also discuss its influence on the yield surface's shape. Additionally, we probe the consequences of slips with the shear thinning/thickening indices on both the plug and shearing velocity profiles along with the flow rate. In the same section, finally we will discuss the flow reversal in the deformable channels and effect of deformability and slip on the plug height.

# 2 Governing equations

## 2.1 Cauchy equations

The Cauchy's equation and the continuity equation for an incompressible fluid are given by

$$\rho\left(\frac{\partial \boldsymbol{v}}{\partial t} + (\boldsymbol{v}\cdot\boldsymbol{\nabla})\boldsymbol{v}\right) = -\boldsymbol{\nabla}p - \rho\boldsymbol{g} + \boldsymbol{\nabla}\boldsymbol{.}\boldsymbol{\tau}, \qquad \boldsymbol{\nabla}\cdot\boldsymbol{v} = 0, \tag{1a,b}$$

where $\boldsymbol{v} = [u, v, w]$ is the fluid velocity, $p$ is the fluid pressure, $\rho$ is the fluid density, $\boldsymbol{g}$ is the gravitational body force, and $\boldsymbol{\tau}$ is the total deviatoric stress tensor.

## 2.2 Boundary conditions

Boundary conditions play an important role in determining the solution. We assume that the fluid cannot penetrate the channel wall. Therefore, on the boundary $\Gamma$

$$\boldsymbol{v}\cdot\boldsymbol{n}_{\text{wall}} = 0, \tag{2}$$

where $\boldsymbol{n}_{\text{wall}}$ is the unit outward normal vector on the wall. Generally, the no-slip boundary condition at the fluid-solid interface is a fundamental notion in fluid mechanics. However, wall-slip is a common phenomenon in yield-stress fluids. Therefore, this requires a certain degree of tangential velocity (Navier slip) in order to match experimental observations [82, 83, 84, 85] . This leads to

$$\Theta \boldsymbol{v}.\boldsymbol{m}_{\text{wall}} + (1-\Theta)\boldsymbol{\tau}\boldsymbol{n}_{\text{wall}}.\boldsymbol{m}_{\text{wall}} = 0, \tag{3}$$

where $\boldsymbol{m}_{\text{wall}}$ is the tangential unit vector along the channel wall. Also, the arbitrary parameter $\Theta$ meets $0 \le \Theta \le 1$. Here, $\Theta = 0$ and 1 correspond to pure-slip and no-slip boundary conditions. The symmetry boundary condition at the centreline of the channel $z = 0$ demands the velocity normal to the centreline and the velocity gradient $\boldsymbol{v_g}$ tangential to the centreline (and with in the plug) are both zero. These two conditions can be expressed as

$$\boldsymbol{v} \cdot \boldsymbol{n}_{\text{centreline}} = 0, \qquad \text{and} \qquad \boldsymbol{v_g} \cdot \boldsymbol{m}_{\text{centreline}} = 0, \tag{4a,b}$$

respectively, where $\boldsymbol{n}_{\text{centreline}}$ and $\boldsymbol{m}_{\text{centreline}}$ are the unit normal and unit tangent vector to the symmetry boundary, respectively.

# 3 The model

## 3.1 Structural mechanics: small displacement mechanics

Gervais et al. [13] performed the scaling analysis and showed that if the top wall is thick and the deformations are shallow, then the internal strains along vertical ($\delta/W$ along $z$ direction) and lateral ($\Delta W/H$) directions are proportional to $p/E$, where $p$ is the pressure and $E$ is the elastic modulus. For $H/W \ll 1$, the strains could be rearranged to $\delta/H = cpW/EH$, where $\delta$ is the change in height due to shallow deformations and $c$ is an unknown constant. Therefore, Gervais et al. [13] approximated, the width–averaged height of the channel along the length as

$$H(x) = H_o\left(1 + \alpha\frac{p(x)W}{EH_o}\right), \tag{5}$$

where $p(x)$ is the pressure at any longitudinal direction $x$ and $0 < \alpha < 2/3$. $H_o$ is the initial height of the channel when $\delta = 0$. However, $\alpha$ is a fitting parameter that varies with the geometry of the channel and needs to be calculated explicitly from experiments. To overcome this issue, [14] performed the perturbation analysis using the isotropic quasi–static plate bending and the Stokes equations. They found that for rectangular cross–section $\alpha = (1/60)(W/\mathcal{T})^3(1-\nu^2)$, where $\mathcal{T}$ is the thickness of the upper horizontal wall and $\mu$ is the Poisson's ratio of the material (for incompressible material $\nu = 0.5$ [86]).

## 3.2 Herschel–Bulkley fluid model

We study the flow of yield stress, shear thinning , and thickening fluids in the flexible channels. To model the fluid behavior, we use the Herschel–Bulkley fluid model, which in one dimension is given by

$$\begin{aligned} \dot{\gamma} = 0, \qquad & \text{if} \qquad \tau < \tau_y \\ \tau = \tau_y + \eta_o \dot{\gamma}^n, \qquad & \text{if} \qquad \tau \geq \tau_y \end{aligned} \tag{6}$$

where $\tau$ and $\tau_y$ are the stress and yield stress, respectively. Here, $\dot{\gamma}$ is the shear-rate and $\eta_o$, $n$ are the consistency and shear-thinning/thickening indexes, respectively. If $n = 1$, the model represents the Bingham model. For $\tau_y = 0$, the model is the power–law fluid. For the cases, $n < 1$ and $n > 1$ represent the shear thinning and shear thickening fluids, respectively. Finally, $\tau_y = 0$ and $n = 1$ represents the Newtonian fluids.

### 3.3 2D planar model

We consider fully developed, steady laminar flow of an incompressible yield stress Hershcel–Bulkley fluid between two parallel plates under lubrication limits in a rectangular channel of height $H$ and width $W$ as shown schematically in Figure 1. The channel is assumed to be sufficiently long and wide in comparison to the height (that is, $H/W \ll 1$, and $H/L \ll 1$) to use a two–dimensional planar model [14, 87, 21]. We further assume a very small displacement due to deformability in comparison to the height of the channel, $\delta/H \ll 1$, which is caused by the pressure difference between the fluid and the atompheric conditions in the deformable channel. The mid–plane between the plates will be taken as the origin with the flow domain extending from $z = -H/2$ to $z = +H/2$.

Further suppose that the Cartesian velocity components $u$ and $w$ along longitudinal and vertical directions $x$ and $z$, respectively. The $z$ coordinate is measured from the channel's mid–plane. Therefore, using the lubrication assumptions in the shallow cross–section of the channel as shown in [14], we retain the leading order terms. Using the impermeable solid–wall boundary condition, we get $w(z = -H(x)/2) = w(z = H(x)/2) = 0$. In the leading order terms, using the impermeable solid-wall boundary condition, the normal velocity vanishes everywhere, that is,

$$w(z, t) = 0. \tag{7}$$

Further, we neglect the pressure gradient and velocity components normal to the channel wall. Also, we neglect all body forces. Under these assumptions, for $H/W \ll 1$, and $H/L \ll 1$, we show a fluid element $ABCDD'A'B'C'$ in Figure 1. The force balance on this element can be calculated as the pressure $p$ and $p + \dfrac{\partial p}{\partial x} dx$ acting on the $AA'D'D$, and $BB'C'C$ surfaces, respectively along the positive and negative $x$ directions. Also, the shear stress $\tau_{xz}$ is acting along the negative $x$ direction on both the surfaces $DD'C'C$ and $AA'B'B$. Dropping the $xz$ notation from the stress, the force balance can be written as [16]

$$2Wpz - 2W\Big(p + \frac{\partial p}{\partial x}\, dx\Big)z = 2W\tau\, dx, \tag{8}$$

which implies

$$\tau = -\frac{\partial p}{\partial x} z, \tag{9}$$

where $\tau$ is the shear stress for the Herschel–Bulkley fluids. From equation (6), $\tau$ is given by

$$\tau = \tau_y + \eta_o \biggl( -\frac{\partial u}{\partial z} \biggr)^n, \tag{10}$$

and $\eta_o$ is a Herschel–Bulkley consistency index (Bingham consistency index for $n = 1$). Using equation (9) and (10), we get

$$-\frac{\partial u}{\partial z} = \frac{1}{\eta_o^{1/n}} \biggl( -\frac{\partial p}{\partial x} z - \tau_y \biggr)^{1/n}. \tag{11}$$

Integrating equation (11), we get

$$-u = \frac{n}{(n+1)} \frac{1}{\eta_o^{1/n} \bigl( -\frac{\partial p}{\partial x} \bigr)} \biggl( -\frac{\partial p}{\partial x} z - \tau_y \biggr)^{(1+n)/n} + c_1, \tag{12}$$

From equation (9), the stress on the upper channel wall is

$$\tau_{\text{wall}} = -\frac{\partial p}{\partial x} \frac{H}{2}, \tag{13}$$

Also, the yield surface $H_p$ or the plug height below which the flow will be like a plug says that at $z = H_p$, $\dfrac{\partial u}{\partial z} = 0$. This implies from equations (9) and (10) that

$$H_p = \tau_y \Bigg/ \biggl( -\frac{\partial p}{\partial x} \biggr). \tag{14}$$

The slip boundary condition says $u = \lambda \left| \dfrac{\partial u}{\partial z} \right|$ at $z = H/2$, where $\lambda = \mu_{\text{vp}}(1 - \Theta)/\Theta \geq 0$ and $\mu_{\text{vp}} = |\tau| \Big/ \left| \dfrac{\partial u}{\partial z} \right|$ is the effective viscoplastic viscosity. Using the slip boundary condition and equations (13) and (14) in equation (12), we get

$$u = \frac{n}{(n+1)} \frac{H}{2} \biggl( \frac{\tau_{\text{wall}}}{\eta_o} \biggr)^{1/n} \Biggl[ \biggl( 1 - 2\frac{H_p}{H} \biggr)^{(1+n)/n} - \biggl( 2\frac{z}{H} - 2\frac{H_p}{H} \biggr)^{(1+n)/n} \Biggr] + \lambda \biggl( \frac{\tau_{\text{wall}}}{\eta_o} \biggr)^{1/n} \biggl( 1 - 2\frac{H_p}{H} \biggr)^{1/n}, \tag{15}$$

From above, the velocity in the plug, that is, $u_p$ at $z = H_p$, is

$$u_p = \frac{n}{(n+1)} \frac{H}{2} \biggl( \frac{\tau_{\text{wall}}}{\eta_o} \biggr)^{1/n} \biggl( 1 - 2\frac{H_p}{H} \biggr)^{(1+n)/n} + \lambda \biggl( \frac{\tau_{\text{wall}}}{\eta_o} \biggr)^{1/n} \biggl( 1 - 2\frac{H_p}{H} \biggr)^{1/n}. \tag{16}$$

It is crucial to emphasize that the equations (15) and (16) governing flow velocities are valid exclusively when $H_p$ is less than or equal to $H/2$. If this condition is not met, both $u$ and $u_p$ become zero within the channel, resulting in a fully plugged fluid without any movement. The volume flow rate in a deformable nanochannel is given by

$$Q = 2W\int_0^{H(x)/2} u dz = 2W\int_0^{H_p} u_p dz + 2W\int_{H_p}^{H(x)/2} u dz, \tag{17}$$

Integrating the right–hand–side of the above equation (17) and using equations (13), (14) with rearrangment, we get

$$Q = \frac{2Wn}{(2n+1)(n+1)}\Bigg(-\frac{\partial p}{\partial x}\frac{1}{2\eta_o}\Bigg)^{1/n}(H-2H_p)^{(n+1)/n}\Bigg(\frac{(n+1)H}{4}+\frac{nH_p}{2}\Bigg) + WH\lambda\Bigg(-\frac{\partial p}{\partial x}\frac{1}{2\eta_o}\Bigg)^{1/n}\Bigg(H-2H_p\Bigg)^{1/n}. \tag{18}$$

Now, from equation (5), that

$$H(x) = H_o\Bigg(1+\alpha\frac{p(x)W}{EH_o}\Bigg) = H_o\Big(1+\beta p(x)\Big), \tag{19}$$

where $\beta = \alpha\dfrac{W}{EH_o}$. Substituting equation (19) in equation (18), we integrate along the channel length $L$ by assuming a constant pressure gradient and a pressure $p(x)$ at $x$ with respect to the pressure at the outlet of the channel, where we assumed the outlet pressure $p(x=L)=0$. This yields

$$\int_x^L Q^n dx = -\Bigg(\frac{2Wn}{(2n+1)(n+1)}\Bigg)^n \frac{1}{2\eta_o}\int_{p(x)}^0 \Big(H_o\Big(1+\beta p(x)\Big)-2H_p\Big)^{n+1}\Bigg(\frac{(n+1)H_o\Big(1+\beta p(x)\Big)}{4} + \frac{nH_p}{2}\Bigg)^n dp. \tag{20}$$

$$\int_x^L Q^n dx = \frac{-W^n}{2\eta_o}\int_{p(x)}^0 \Big(H_o\Big(1+\beta p(x)\Big)-2H_p\Big)\Bigg[\Bigg(\frac{2n}{(2n+1)(n+1)}\Bigg)\Bigg(\frac{(n+1)H_o\Big(1+\beta p(x)\Big)}{4} + \frac{nH_p}{2}\Bigg)\Big(H_o\Big(1+\beta p(x)\Big)-2H_p\Big)+\lambda H_o\Big(1+\beta p(x)\Big)\Bigg]^n dp. \tag{21}$$

The term in big-square bracket in above equation (21) can be re-written as

$$\Bigg[\left(\frac{2n}{(2n+1)(n+1)}\right)\left(\frac{(n+1)H_o\Big(1+\beta p(x)\Big)}{4}+\frac{nH_p}{2}\right)\Big(H_o\Big(1+\beta p(x)\Big)-2H_p\Big) \\ +\lambda H_o\Big(1+\beta p(x)\Big)\Bigg]^n=\Bigg[\zeta+\theta\beta p(x)+\phi(\beta p(x))^2\Bigg]^n, \tag{22}$$

where

$$\zeta=\left(\frac{n}{2(2n+1)(n+1)}\right)\Big((n+1)H_o+2nH_p\Big)\Big(H_o-2H_p\Big)+\lambda H_o, \tag{23}$$

$$\theta=\left(\frac{n}{(2n+1)(n+1)}\right)\Big((n+1)H_o^2-H_oH_p\Big)+\lambda H_o, \tag{24}$$

and

$$\phi=\left(\frac{2n}{(2n+1)(n+1)}\right)\left(\frac{(n+1)H_o^2}{4}\right), \tag{25}$$

There will now be two asymptotic limits of the integral in equation (21).

**Case 1:** Under small displacement assumption, where $\beta p(x)\ll 1$ such that $\frac{\theta}{\zeta}\beta p(x)\ll 1$, and $\frac{\phi}{\zeta}\beta p(x)\ll 1$, therefore the expression in the integral can we approximated to the leading order of $\beta p(x)$ as

$$\Big(H_o\Big(1+\beta p(x)\Big)-2H_p\Big)\Bigg[\zeta+\theta\beta p(x)+\phi(\beta p(x))^2\Bigg]^n \\ =\zeta^n\Bigg[(H_o-2H_p)+\left(H_o+(H_o-2H_p)\frac{n\theta}{\zeta}\right)\beta p(x)\Bigg]+O((\beta p(x))^2)+.... \tag{26}$$

Using the leading order terms of the integral from equation (26) in equation (21), we get

$$Q^n(L-x)=\frac{\zeta^nW^n}{2\eta_o}p(x)\left((H_o-2H_p)+\left(H_o+(H_o-2H_p)\frac{n\theta}{\zeta}\right)\beta\frac{p(x)}{2}\right). \tag{27}$$

Using $x = 0$, where $p(x) = p_{\text{in}} = -\Delta p$ (as $p_{\text{x=L}} = 0$), we rewrite the above expression as

$$Q = W\zeta(H_o - 2H_p)^{1/n}\left(\frac{-\Delta p}{2\eta_o L}\right)^{1/n}\left(1 + \underbrace{\left(\frac{H_o}{(H_o - 2H_p)} + \frac{n\theta}{\zeta}\right)\beta\frac{(-\Delta p)}{2}}_{\mathcal{X}}\right)^{1/n}. \tag{28}$$

It is important to highlight that equation (28) governing the volume flow rate is valid for $H_p \leq H/2$. Otherwise, the flow is completely choked in the channel.

**Case 2:** We have another asymptotic limit, where $\beta p(x) \gg 1$ such that $\dfrac{\theta}{\zeta}\beta p(x) \gg 1$, and $\dfrac{\phi}{\zeta}\beta p(x) \gg 1$. In this limit, the perturbation due to flexibility is large and the predicted flow rate can have large errors. Under this limit, the expression in the integral in equation (21) can be approximated to

$$\Big(H_o\Big(1 + \beta p(x)\Big) - 2H_p\Big)\Big[\zeta + \theta\beta p(x) + \phi(\beta p(x))^2\Big]^n \approx \phi^n \ H_o(\beta p(x))^{2n+1}. \tag{29}$$

Using the leading order terms of the integral from equation (29) in equation (21), we integrate, which gives the flow rate as

$$Q^n(L - x) = \frac{W^n}{4(n+1)\eta_o}\phi^n \ H_o\beta^{2n+1}(p(x))^{2n+2}. \tag{30}$$

Using $x = 0$, where $p(x) = p_{\text{in}} = -\Delta p$ (as $p_{\text{x=L}} = 0$), we rewrite the above expression as

$$Q = \left(\frac{W^n}{4(n+1)\eta_o L}\phi^n \ H_o\beta^{2n+1}(-\Delta p)^{2n+2}\right)^{1/n}. \tag{31}$$

## 3.4 Limiting cases

### 3.4.1 For the Bingham fluid flow with slip in the flexible channel: $n = 1$

Using equation (28) under small displacement assumption, for the Bingham fluid flow with slip in the deformable channel, that is, $n = 1$, we get

$$Q = W\zeta(H_o - 2H_p)\left(\frac{-\Delta p}{2\eta_o L}\right)\left(1 + \left(\frac{H_o}{(H_o - 2H_p)} + \frac{\theta}{\zeta}\right)\beta\frac{(-\Delta p)}{2}\right), \tag{32}$$

where

$$\zeta = \left(\frac{1}{12}\right)\Big(2H_o + 2H_p\Big)\Big(H_o - 2H_p\Big) + \lambda H_o, \tag{33}$$

$$\theta = \left(\frac{1}{6}\right)\left(2H_o^2 - H_o H_p\right) + \lambda H_o. \tag{34}$$

To the best of our knowledge, we have not seen the above derived equation (32) in the literature so far.

#### 3.4.2 For the Herschel-–Bulkley fluid flow without slip in the flexible channel: $\lambda = 0$

Using equation (28) under small displacement assumption, for the Herschel-–Bulkley fluid flow without slip, that is, $\lambda = 0$, we get

$$\begin{aligned} Q = \frac{2Wn}{(2n+1)(n+1)}\left(\frac{-\Delta p}{2\eta_o L}\right)^{1/n}\Bigg[&(H_o - 2H_p)^{(n+1)/n}\left(\frac{(n+1)H_o + 2nH_p}{4}\right) \\ &\left(1 + \frac{(n+1)\beta(-\Delta p)H_o}{2(H_o - 2H_p)} + \frac{n(n+1)H_o\beta(-\Delta p)}{2(n+1)H_o + 4nH_p}\right)^{1/n}\Bigg]. \end{aligned} \tag{35}$$

The above expression (35) is also derived by Garg and Prasad [12] for $\beta|\Delta p| \ll 1$.

#### 3.4.3 For the Bingham fluid flow without slip in the flexible channel: $n = 1$, $\lambda = 0$

Using equation (28) under small displacement assumption, for the Bingham fluid flow without slip, that is, $n = 1$ and $\lambda = 0$, we get

$$Q = \frac{W}{12}\left(\frac{-\Delta p}{\eta_o L}\right)\left[\left(H_o - 2H_p\right)^2\left(H_o + H_p\right)\left(1 + \frac{3H_o^2}{(H_o - 2H_p)(H_o + H_p)}\frac{\beta(-\Delta p)}{2}\right)\right]. \tag{36}$$

The above expression (36) is also derived by Garg and Prasad [12] for $\beta|\Delta p| \ll 1$.

#### 3.4.4 For the Newtonian fluid flow with slip in flexible channel: $n = 1$, $H_p = 0$

Similarly, using equation (28) under small displacement assumption, for the Newtonian fluid flow with slip, that is, $n = 1$, $\tau_y = 0 \implies H_p = 0$, we get

$$Q = \frac{W}{12}\left(\frac{-\Delta p}{\eta_o L}\right)H_o^3\left[\left(1 + \frac{3\beta(-\Delta p)}{2}\right) + \frac{6\lambda}{H_o}\left(1 + \beta(-\Delta p)\right)\right]. \tag{37}$$

The above expression (37) is also derived by Garg [15] for $\beta|\Delta p| \ll 1$.

### 3.4.5 For the Newtonian fluid flow without slip in flexible channel: $n = 1$, $H_p = 0$, $\lambda = 0$

Similarly, using equation (28) under small displacement assumption, for the Newtonian fluid flow without slip, that is, $n = 1$, $\lambda = 0$, $\tau_y = 0 \implies H_p = 0$, we get

$$Q = \frac{W}{12}\left(\frac{-\Delta p}{\eta_o L}\right) H_o^3 \left(1 + \frac{3\beta(-\Delta p)}{2}\right). \tag{38}$$

The above expression (38) is also derived by Gervais et al. [13], Christov et al. [14], Garg [15], Garg and Prasad [12] for $\beta|\Delta p| \ll 1$.

### 3.4.6 For the Herschel–Bulkley fluid flow in the rigid channel: $\beta = 0$

Using equation (28) under small displacement assumption, for the Herschel–Bulkley fluid flow in the rigid channel, that is, $\beta = 0$, we get

$$Q = \frac{2Wn}{(2n+1)(n+1)}\left(\frac{-\Delta p}{2\eta_o L}\right)^{1/n}\left[\left(H_o - 2H_p\right)^{(n+1)/n}\left(\frac{(n+1)H_o + 2nH_p}{4}\right)\right]. \tag{39}$$

A similar expression, but for the Bingham fluid flow in the rigid channel is given in Chhabra and Richardson [16].

### 3.4.7 For the Bingham fluid flow in the rigid channel: $\beta = 0$, $n = 1$

Using equation (28), for the Bingham fluid flow in the rigid channel, we get

$$Q = \frac{W}{12}\left(\frac{-\Delta p}{\eta_o L}\right)\left(H_o - 2H_p\right)^2\left(H_o + H_p\right), \tag{40}$$

which is also given in Chhabra and Richardson [16].

### 3.4.8 For the power-law fluid flow in the rigid channel: $\beta = 0$, $\tau_y = 0$

Using equation (28), for the power-law fluid flow in the rigid channel, we get

$$Q = \frac{H_o W n}{(2n+1)}\left(\frac{1}{2}\right)^{(1+n)/n}\left(\frac{-\Delta p}{\eta_o L}\right)^{1/n}\left(H_o\right)^{(n+1)/n}, \tag{41}$$

which is also given in Chhabra and Richardson [16].

### 3.4.9 For the Newtonian fluid flow in the rigid channel: $\beta = 0$, $n = 1$, $H_p = 0$

Using equation (28), for the Newtonian fluid flow in the rigid channel, we get

$$Q = \frac{W}{12}\left(\frac{-\Delta p}{\eta_o L}\right) H_o^3, \tag{42}$$

which is a classical result of Hagen-Poiseuille flow in channels as given in [88, 89, 90, 16, 15].

# 4 Results and discussion

## 4.1 Effect of yield stress on the flow in the rigid and deformable channel with and without wall-slip

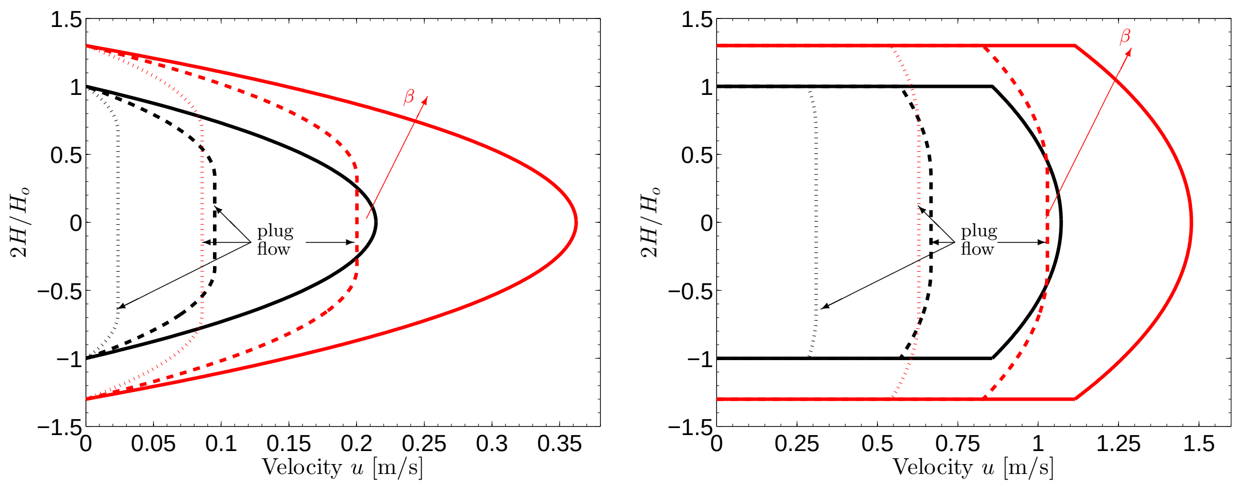


Figure 2: Velocity profiles at varying yield stress for the rigid ($\beta = 0$ in black) and deformable ($\beta = 0.005$ in red) channels. The solid line, dashed line, and dotted lines show the data at yield stress values of 0 Pa, 2 Pa, and 4 Pa, respectively. In (a) $\lambda = 0$ (Taken from Garg and Prasad [12], although using these parameters with $\lambda = 0$, we can also calculate the same using the current model derived in this paper) and in (b) the slip-length $\lambda = 0.1$ m.

For the discussions in the results section, we set $H_o = 0.1$ m, $L = 0.5$ m, $W = 1$ m, and $\eta_o = 0.7$ Pa everywhere. From equation (14), we calculate the values of plug height as $H_p = \tau_y L/|\Delta p|$. Using equations (15) (for $z > H_p$) and (16) (for $0 \leq z \leq H_p$), we show the velocity profiles at $|\Delta p| = 60$ Pa, $n = 1$ at varying yield stress for the rigid ($\beta = 0$ Pa$^{-1}$ in the black color), and deformable ($\beta = 0.005$ Pa$^{-1}$ in the red color) channels in Figure 2(a,b).

The solid line, dashed line, and dotted lines show the data at yield stress values of $\tau_y = 0$ Pa, $\tau_y = 2$ Pa, and $\tau_y = 4$ Pa, respectively in both figures (a) and (b). In (a) $\lambda = 0$ (Taken from Garg and Prasad [12], please note that we can also calculate the same using the current model derived in this paper with $\lambda = 0$) and in (b) the slip-length $\lambda = 0.1$ m. We find that due to flexibility ($\beta = 0.005$ Pa$^{-1}$) in the channel, the channel height increases by 30% for both slip lengths.

Further, for $\tau_y = 0$ Pa, we find that as the deformability parameter increases from 0 to 0.005 Pa$^{-1}$, the maximum velocity at the centerline increases from approximately 0.21 m/s to 0.36 m/s for $\lambda = 0$, whereas it increases from approximately 1.1 m/s to 1.5 m/s for $\lambda = 0.1$ m. This trend has been found at non–zero yield stress values too. This suggests irrespective of yield stress and deformability parameter, the slip increases the velocity and wall-slip shifts the flow curve to the right. Due to increased velocity, the flow rate also increases. In the presence of yield stress, the velocity profiles are divided into two parts, the plug velocity within the central region where the bulk of the fluid moves with a constant velocity as a solid material. On the other hand, for $z > H_p$, the velocity profile is dictated as the fluid is flowing normally with finite shear stresses ($> \tau_y$). We refer the flow profile discussion when the slip effects are absent from [12]. For $\lambda = 0.1$ m and $\tau_y = 2$ Pa, the centerline plug velocity increases from 0.65 m/s in the rigid channel to 1 m/s in the deformable channel with $\beta = 0.005$ Pa$^{-1}$ as shown in Figure 2(b) with dashed black and red lines respectively. A similar increment due to deformation is found at $\tau_y = 4$ Pa. This indicates that the deformability increases the velocity and hence the flow rate in the deformable channel for a given pressure and material properties. We also find that as the yield stress is increasing, the plug height keeps increasing and the maximum velocity decreases which also decreases the flow rate in the channel. This trend is the same with and without wall-slip. We also find that the slip has no effect on the height increment of the channel due to deformability.

### 4.2 Effect of shear-thinning/thickening on the flow in the rigid and deformable channel with and without wall-slip

We show the velocity profiles at $|\Delta p| = 60$ Pa, $\tau_y = 2$ Pa at varying shear thinning/thickening index $n$ for the rigid ($\beta = 0$ Pa$^{-1}$ in the black color), and deformable ($\beta = 0.005$ Pa$^{-1}$ in the red color), channels in Figure 3(a,b). The solid line, dashed line, and the dotted lines show the data at shear thinning/thickening index $n$ of $n = 0.8$, $n = 1$, and $n = 1.2$, respectively. In (a) $\lambda = 0$ (Taken from Garg and Prasad [12], please note that we can also calculate the same using the current model derived in this paper with $\lambda = 0$) and in (b) the slip-length $\lambda = 0.1$ m. The central region within the dashed blue line indicates the plug flow region.

We find that due to non–zero yield stress in all predictions, the velocity profiles are divided into two parts, the plug velocity in the central region and the normal shearing velocity towards

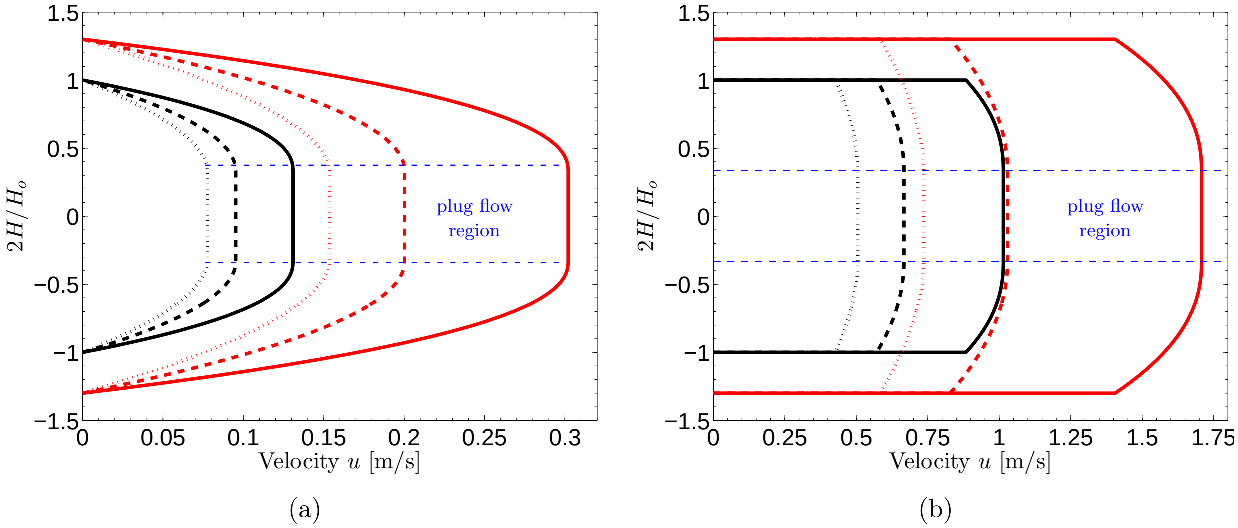


Figure 3: Velocity profiles at varying shear thinning and thickening index for the rigid ($\beta = 0$ in black) and deformable ($\beta = 0.005$ in red) channels. The solid line, dashed line, and dotted lines show the data at shear thinning/thickening index values of $n = 0.8$, $n = 1$, and $n = 1.2$, respectively. In (a) $\lambda = 0$ (Taken from Garg and Prasad [12], please note that we can also calculate the same using the current model derived in this paper with $\lambda = 0$) and in (b) the slip-length $\lambda = 0.1$ m. The central region within the dashed blue line indicates the plug flow region.

the channel wall. For $n = 1$ (Bingham fluid), as the deformability parameter increases from 0 to 0.005 $\mathrm{Pa}^{-1}$, the maximum velocity at the centerline increases from approximately 0.09 m/s to 0.2 m/s for $\lambda = 0$, whereas it increases from approximately 1.1 m/s to 1.5 m/s for $\lambda = 0.1$ m as shown with dashed lines. This trend has been found in shear thinning ($n = 0.8$) and shear thickening ($n = 1.2$) materials too. This suggests irrespective of yield stress and deformability parameter, the slip increases the velocity and wall-slip shifts the flow curve to the right. Due to increased velocity, the flow rate also increases. We refer the flow profile discussion when the slip effects are absent from [12]. For $\lambda = 0.1$ m and $n = 0.8$, the centerline plug velocity increases from 0.65 m/s in the rigid channel to 1 m/s in the deformable channel with $\beta = 0.005$ $\mathrm{Pa}^{-1}$ as shown in Figure 3(b) with dashed black and red lines respectively. A similar increment due to deformation is found at $n = 1.2$. This indicates that the deformability increases the velocity and hence the flow rate in the deformable channel for a given pressure and material properties. We also find that as the shear thinning/thickening index $n$ is increasing, although the plug height remains the same but the maximum velocity decreases which also decreases the flow rate in the channel. This trend is the same with and without wall-slip. We also find that the slip has no effect on the plug height. Further, we find that, the slip has no effect on the channel height increment due to deformability.

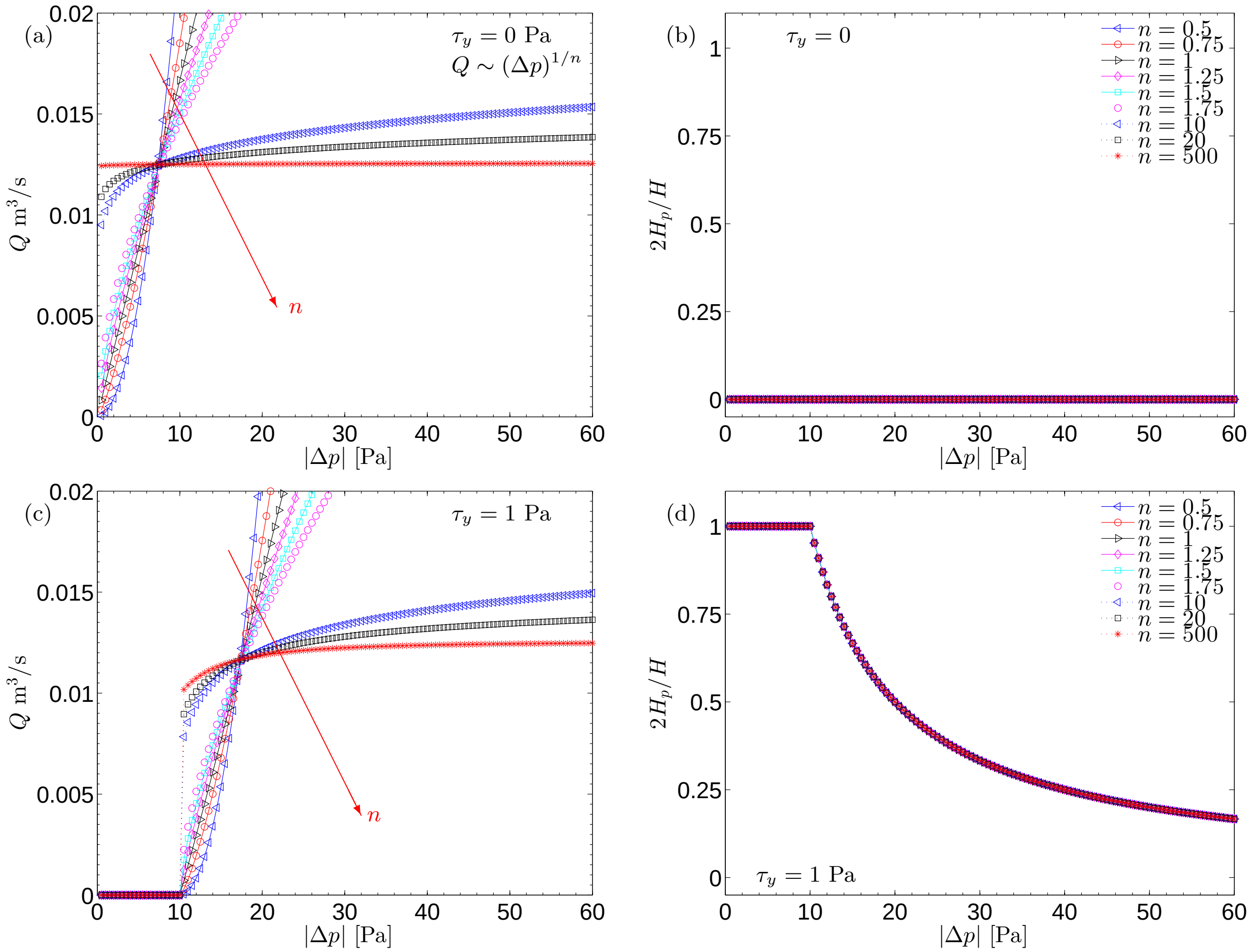


Figure 4: We show the flow rate (with $\lambda = 0.1$ m) in the rigid ($\beta = 0$ Pa$^{-1}$) channel at varying $|\Delta p|$, and shear thinning/thickening index $n$ at $\tau_y = 0$ Pa in (a), and $\tau_y = 1$ Pa in (c), respectively. The red arrow indicates the increasing values of shear thinning/thickening index $n$ with 0.5, 0.75, 1, 1.25, 1.5, 1.75, 10, 20, and 500 from blue triangle to red circles, respectively. In Figures (b) and (d), we show the corresponding plug height with varying pressure for all $n$ at $\tau_y = 0$ Pa, and $\tau_y = 1$ Pa, respectively.

### 4.3 Effect of yield stress and shear thinning/thickening index on the flow rate in the rigid channel with wall-slip

Using equation (28) with $\lambda = 0.1$ m, we calculate the flow rate in the rigid ($\beta = 0$ Pa$^{-1}$) channel at varying $|\Delta p|$ and shear thinning/thickening index $n$ at $\tau_y = 0$ Pa in Figure 4(a) and $\tau_y = 1$ Pa in Figure 4(c), respectively. The red arrow indicates the increasing values of shear thinning/thickening index $n$ with values 0.5, 0.75, 1, 1.25, 1.5, 1.75, 10, 20, and 500 from blue triangle to red circles, respectively. We find that for $n < 1$, the flow rate curve is like an upward parabola, whereas for $n = 1$, it is a straight line and $n > 1$, it is a rightward parabola. Due to that, for $|\Delta p| \leq 10$ Pa, the flow rate for $n < 1$ is lower than for $n > 1$, whereas it becomes the opposite for $|\Delta p| > 10$ Pa. In the case of a rigid channel wall, the flow rate scales as $Q \sim (|\Delta p|)^{1/n}$. We find that for $n = 10, 20$, $Q$ is significantly dependent on $|\Delta p|$, whereas in case of no-slip (that is $\lambda = 0$ m), it was weakly dependent as observed by Garg and Prasad [12]. Further at $|\Delta p| \approx 0$, the flow rate is significant with slips, whereas it was one-third of it, when slip was not considered by Garg and Prasad [12]. We also find that as the $n \gg 1$ such as for $n = 500$ (shown with red asterisk), the flow rate becomes independent to $|\Delta p|$. This behaviour is consistent with the scaling also, where $Q \sim (|\Delta p|)^{1/n}$ and as $n \implies \infty$, $Q \sim (|\Delta p|)^0$ . In Figure 4(b), we show the corresponding plug height with varying pressure for all $n$. We find that for $\tau_y = 0$ Pa, $H_p = 0$ for all $n$ and the data collapse on the same line. This behaviour is the same as when the slip was absent as observed by Garg and Prasad [12].

On the other hand for $\tau_y = 1$ Pa in Figure 4(c), we observe that below $|\Delta p| = 10$ Pa, $H_p = H_o/2$. Thus, the material inside the channel is plugged and cannot flow, hence it shows no flow rate. As the pressure difference increases, the flow rate starts to build and show similar trends as in Figure 4(a). We find that for $n = 10,\ 20$, $Q$ is significantly dependent on $|\Delta p|$, whereas in case of no-slip (i.e. $\lambda = 0$ m), it was weakly dependent as observed by Garg and Prasad [12]. Further at $|\Delta p| \approx 10$, the flow rate is significant with slips while it was zero when slip was not considered by Garg and Prasad [12]. We also observe that for given $|\Delta p|$ and $n$, the flow rate decreases as yield stress is increased. We show the corresponding plug height at $\tau_y = 1$ Pa with varying pressure for all $n$ in Figure 4(d). We see that the plug height $H_p$ collapse on the same curve for all $n$. We also find that for $\tau_y = 1$ Pa, $H_p = H_o/2$ for $|\Delta p| \leq 10$ Pa. As the pressure increases the $H_p$ monotonically decreases as $H_p \sim |\Delta p|^{-1}$, which is consistent with equation (14). This behaviour is the same as when the slip was absent as observed by Garg and Prasad [12]. Further, the shear thinning/thickening index does not affect the plug height in the presence of slips, which is same as when the slip was absent as predicted in Garg and Prasad [12]. This behaviour is also consistent with what we saw in the velocity profiles in the previous section 4.2.

### 4.4 Effect of yield stress and shear-thinning/thickening index on the flow rate in the deformable channel with wall-slip

Using equation (28) with $\lambda = 0.1$ m, we calculate the flow rate in the deformable ($\beta = 0.005$ Pa$^{-1}$) channel at varying $|\Delta p|$, and shear thinning/thickening index $n$ at $\tau_y = 0$ Pa in Figure 5(a) and $\tau_y = 1$ Pa in Figure 5(c), respectively. The red arrow indicates the increasing values of shear thinning/thickening index $n$ with 0.5, 0.75, 1, 1.25, 1.5, 1.75, 10, 20, and 500 from blue triangle to red circles, respectively. We find that for $n < 1.75$, the flow rate curve is like an upward parabola, whereas for $n = 1.75$, it is a straight line, and $n > 1.75$, it is a right-

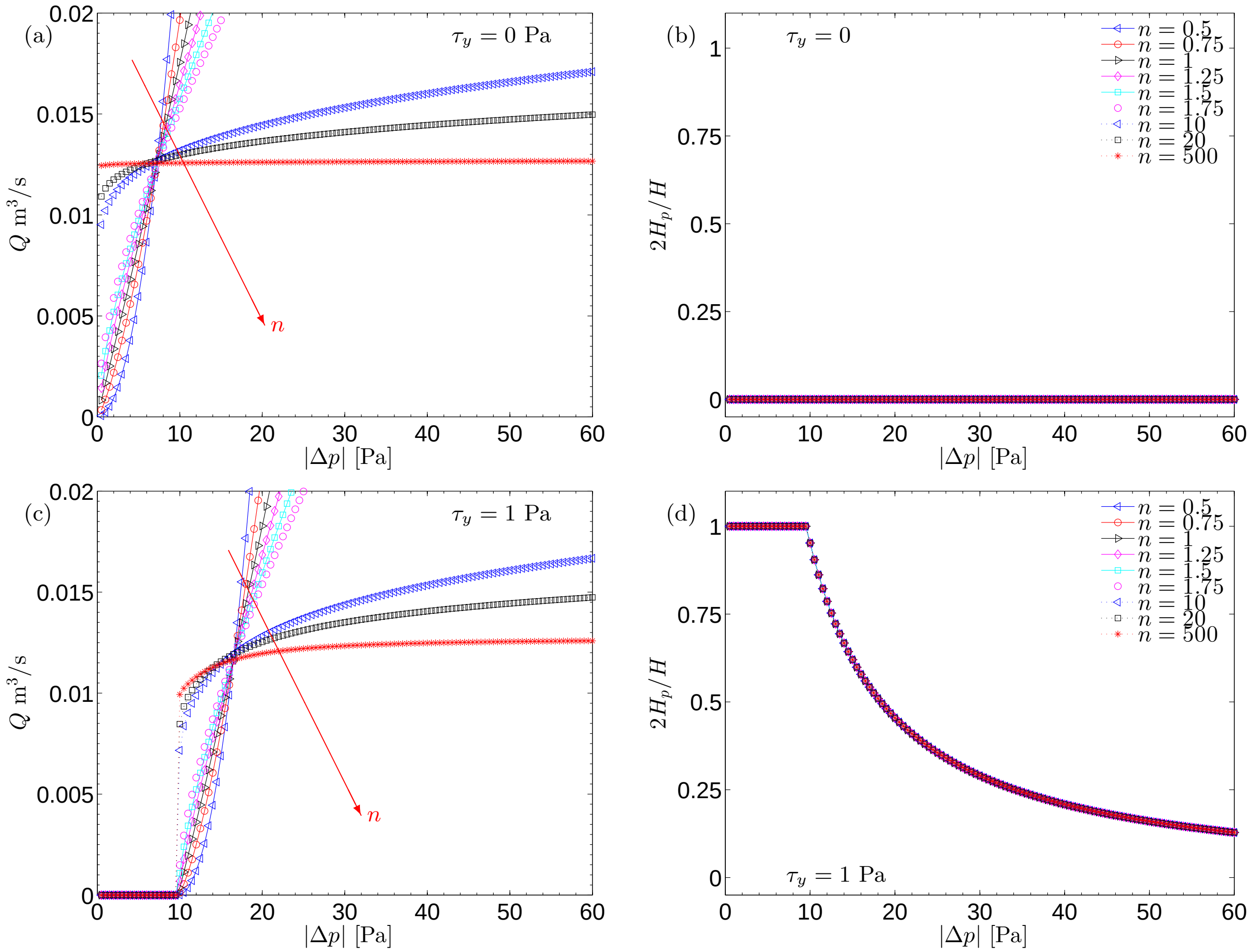


Figure 5: We show the flow rate (with $\lambda = 0.1$ m) in the deformable ($\beta = 0.005$ Pa$^{-1}$) channel at varying $|\Delta p|$, and shear thinning/thickening index $n$ at $\tau_y = 0$ Pa in (a), and $\tau_y = 1$ Pa in (c), respectively. The red arrow indicates the increasing values of shear thinning/thickening index $n$ with 0.5, 0.75, 1, 1.25, 1.5, 1.75, 10, 20, and 500 from blue triangle to red circles, respectively. In Figures (b) and (d), we show the corresponding plug height with varying pressure for all $n$ at $\tau_y = 0$ Pa and $\tau_y = 1$ Pa, respectively.

ward parabola. We see that for $n = 10,\ 20$, the $Q$ is significantly dependent on $|\Delta p|$ whereas in case of no-slip (i.e. $\lambda = 0$ m), it was weakly dependent as observed by Garg and Prasad [12]. Further at $|\Delta p| \approx 0$, the flow rate is significant with slips whereas it was one-third of it, when slip was not considered by Garg and Prasad [12]. In case of deformable wall channel, the flow rate scales as $Q \sim (|\Delta p|)^{1/n}$ for $\mathcal{X} \lesssim O(10^{-1})$ (the $\mathcal{X}$, which is shown as the under–brace term in equation (28). On the other hand the flow rate scales as $Q \sim (|\Delta p|)^{2/n}$ for $\mathcal{X} \sim O(10^0)$. We truncated our expansion in equation (26) because of the small displacement deformability, otherwise for much larger pressure, we need to take those terms into account which gives the scaling as $Q \sim (|\Delta p|)^{2+2/n}$ as shown in equation (31) (although the theory could predict large errors in this asymptotic limit. For $n = 1$, we find that the flow rate $Q \sim (|\Delta p|)^4$, which is consistent as found in [14, 13, 15]). In Figure 5(b), we show the corresponding plug height with varying pressure for all $n$. Also, for $\tau_y = 0$ Pa, $H_p = 0$. This behaviour is the same as when the slip was absent as observed by Garg and Prasad [12].

On the other hand for $\tau_y = 1$ Pa in Figure 5(c), we observe that below $|\Delta p| = 10$ Pa, $H_p = H/2$, similar to as in the case of no-slip (i.e. $\lambda = 0$ m) where the complete material inside the channel is plugged and can not flow. For slightly higher pressure from 10 Pa, we find that, as the pressure difference increases, the flow rate starts to abruptly build and show similar trends as in Figure 5(a). We find that for $n = 10,\ 20$, the $Q$ is significantly dependent on $|\Delta p|$ whereas in case of no-slip (i.e. $\lambda = 0$ m), it was weakly dependent as observed by Garg and Prasad [12]. We further find that for given $|\Delta p|$, and $n$, the flow rate decreases as yield stress is increased similar to as in the case of $\lambda = 0$. We show the corresponding plug height at $\tau_y = 1$ Pa with varying pressure for all $n$ in Figure 5(d). We find that for $\tau_y = 1$ Pa, $H_p = H/2$ for $|\Delta p| \leq 10$ Pa similar to as in the case of no-slip, as predicted in Garg and Prasad [12]. This suggests that slip does not affect the yield surface/ plug height. As the pressure increases, $H_p$ monotonically decreases as $H_p \sim |\Delta p|^{-1}$. We also find that in the case of the deformable channel as well, the shear thinning/thickening index does not affect the plug height in the presence of slips, which is same as when the slip was absent as predicted in Garg and Prasad [12]. This is also consistent with what we saw in the velocity profiles in the previous section 4.2. On comparison of Figure 4(a,c), and 5(a,c), we further find that at given pressure and material properties, due to deformability, the flow rate increases with and without slips, but with slips the flow rate increases more than without slips.

### 4.5 Back/reversal flow in the deformable channel

We show the flow rate (with $\lambda = 0$ m) in the deformable ($\beta = 0.005$ Pa$^{-1}$) channel at varying $|\Delta p|$, and shear thinning/thickening index $n$ at $\tau_y = 4$ Pa in Figure 6(a). We find that the $H_p > H/2$ for pressure upto $|\Delta p| = 35$ Pa. In this regime, the flow is completely choked and $Q = 0$. Further, when we increase the pressure in the range between 35 Pa to 40 Pa, the plug height in the channel becomes $H_o/2 < H_p < H/2$. As we know at the outlet of the channel pressure is assumed to be zero (that is $p(x = L) = 0$), which gives the outlet deformable channel height as $H_o/2$. Also, the deformable channel height due to elasticity between the reservoir and the outlet is greater than the $H_o/2$ (as $p(x \neq L) \neq 0$). Due to that in this flow regime, the outlet of the channel is completely blocked by the plug height. On the other hand, the flow comes in from the reservoir as the plug height at the reservoir is less than the height $H(x = 0)/2$ of the channel. We believe that when the elastic wall of the channel becomes blocked at the outlet, it creates a pressure buildup due to the blockage. As the fluid might not readily deform

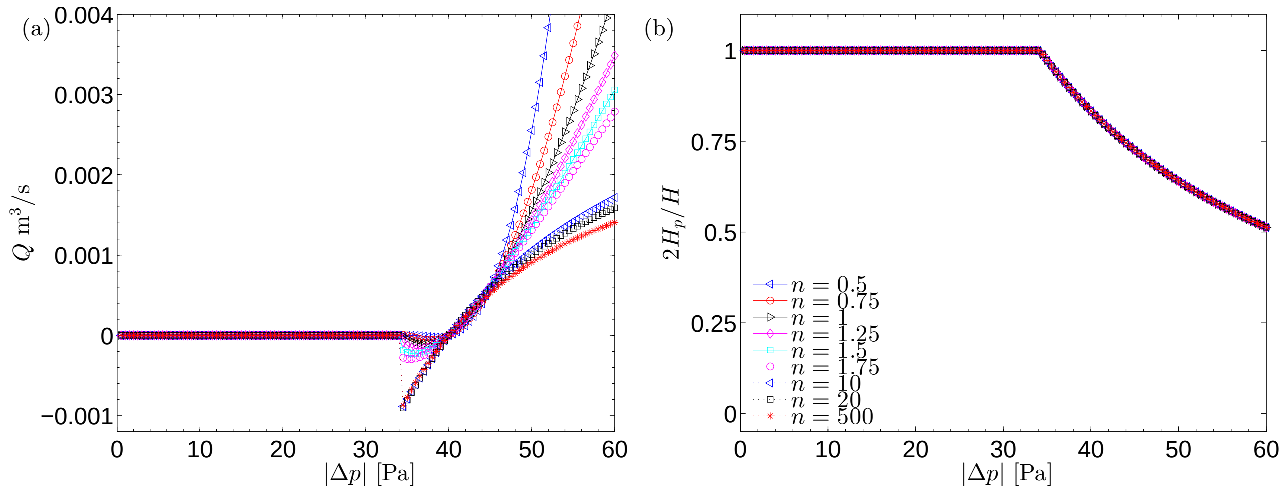


Figure 6: We show the flow rate (with $\lambda = 0$ m) in the deformable ($\beta = 0.005$ Pa$^{-1}$) channel at varying $|\Delta p|$, and shear thinning/thickening index $n$ at $\tau_y = 4$ Pa in (a). In Figure (b), we show the corresponding plug height with varying pressure for all $n$.

or flow out in the direction of outlet, it moves in the reverse direction where the walls are wider and have less resistance to the flow. Further, as the pressure is increased beyond 40 Pa in the reservoir, the plug height becomes less than the outlet height of the channel (i.e. $H_p < H_o/2$). In this flow regime the outlet blockage is removed and the flow starts to move normally in the forward direction. If we further increase the pressure, the flow rate increases normally with the same trend with the pressure as observed and discussed in the previous section too.

In Figure 6(b), we show the corresponding plug height with varying pressure for all $n$. We find that as the yield stress increases to 4 Pa, the flow is completely choked upto 35 Pa, whereas it was choked upto 10 Pa for $\tau_y = 1$ Pa as shown in figure 5(d). Further increment in pressure decreases the plug height, but we find that in comparison to $\tau_y = 1$ Pa, the plug height is more for $\tau_y = 4$ Pa. We will discuss the effect of slip and deformability on the plug height in the next section.

### 4.6 Effect of wall-slip and deformability

We study the variation of plug height in this section. In Figure 7, we show the plug height in the rigid channel (in (a)) and in the deformable ($\beta = 0.005$ Pa$^{-1}$) channel (in (b)), respectively. We calculated the plug height using both $\lambda = 0$ m and $\lambda = 0.1$ m for $n = 0.5$ at varying $|\Delta p|$ for the yield stress between 0 (in black) to 5 Pa (in green). The curves for the rigid and deformable channels for both $\lambda = 0$ m and $\lambda = 0.1$ m superimpose on each other for both the rigid and the deformable channels. This suggests that the slip does not affect the plug height in both the

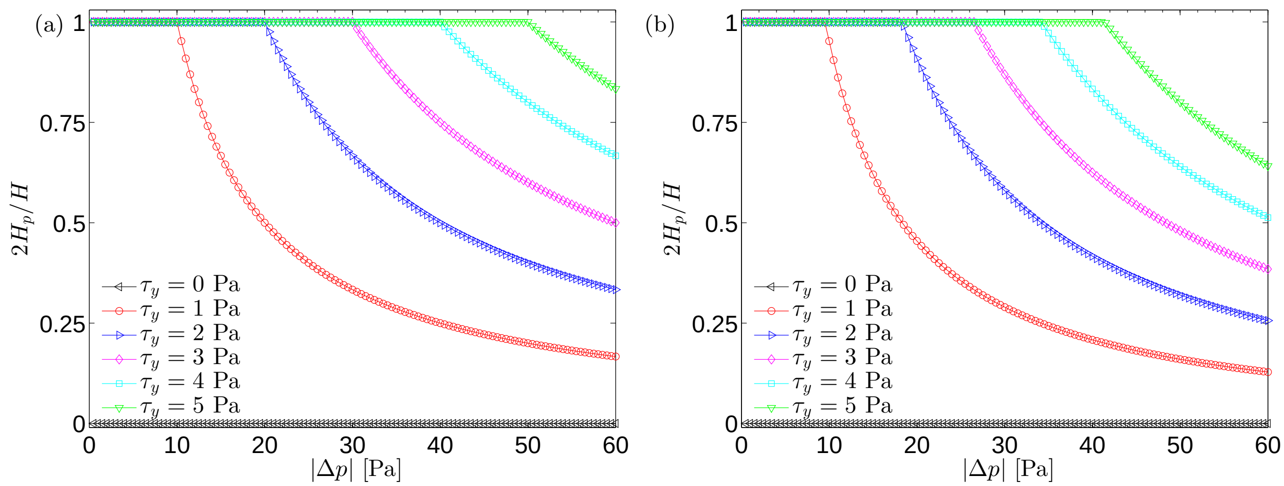


Figure 7: We show the plug height at both $\lambda = 0$ m and $\lambda = 0.1$ m for the $n = 0.5$ in the rigid channel (in (a)) and in the deformable ($\beta = 0.005$ Pa$^{-1}$) channel (in (b)) at varying $|\Delta p|$ for the yield stress between 0 (in black) to 6 Pa (in green).

rigid and the deformable channels. We observed that the plug height is zero for $\tau_y = 0$ Pa in both the rigid and the deformable channels as shown with black data curve. We find that as $\tau_y$ increases the $2H_p/H$ remains one for larger magnitude of the applied pressure. This is because the $H_p \propto \tau_y$. By comparing the plug height in rigid and deformable channels, we find that at a given yield stress, the $|\Delta p|_{\text{deformable}} < |\Delta p|_{\text{rigid}}$ at which the flow is completely choked with $2H_p/H = 1$.

Beyond choked flow, the plug height starts to decrease with $H_p = 1/|\Delta p|$ for both the rigid and the deformable channels. We find that for any given applied pressure and yield stress, the $(H_p)_{\text{deformable}} < (H_p)_{\text{rigid}}$. This behaviour suggest that deformable elastic walls decrease the plug region as well as an early onset of flow with the pressure in comparison to the rigid channel. On the other hand, as stated earlier, the wall-slip has no effect on the plug region and the onset of flow.

## 5 Conclusion

In this paper, we derived analytical model for the velocity profiles and volumetric flow rate in rigid and deformable channels for the shear thinning and shear thickening yield stress materials by considering slips. We focus on investigating the impact of many factors such as the deformability of the channel wall, yield stress, shear thinning, and shear thickening index when slip was present and compared it with flow dynamics with no-slips as reported by Garg and Prasad [12]. In these derivations, we used the small displacement structural mechanics and perturbation theory presented by Gervais et al. [13], and Christov et al. [14], respectively for the constitutive relations of the elastic nature of the channel–walls. We assumed the lubrication assumption in the shallow channels, where the flow velocity profile is assumed to be determined locally by the fluid rheology and the size of the local cross–sectional area. The newly derived model facilitate the flow dynamics of Newtonian fluids, power–law fluids, Bingham fluids, and shear thinning and thickening yield stress fluids with and without slips as its limiting cases. For validation, several sensible trends have been observed. These include the exact derived expression to their corresponding rigid channel–wall formulas given in literature [13, 14, 15, 16] for the Bingham fluids, power–law fluids and the Newtonian fluids. Thorough tests have revealed that the newly derived model produce mathematically and physically sensible results in diverse situations of fluid rheology, shallow channel geometry, and boundary conditions and able to predict in a great extent the effect of slips to the flow dynamics of these.

We also examined the influence of the deformability of the wall on the yield stress fluid flows behavior in the presence of slips within the channels. We found that the deformability increases the effective channel height and the flow rate in the channel. Also, the slip increase both the velocity and the flow rate. In case of deformable wall channel with slips, the flow rate scales as $Q \sim (|\Delta p|)^{1/n}$ for $\mathcal{X} \lesssim O(10^{-1})$ (the $\mathcal{X}$ is shown as the under–brace term in equation (28)), on the other hand the flow rate scales as $Q \sim (|\Delta p|)^{2/n}$ for $\mathcal{X} \sim O(10^0)$. Further, for the large perturbations, the flow rate scales as $Q \sim (|\Delta p|)^{2+2/n}$ (although the theory could predict large errors in this asymptotic limit, and for $n = 1$, we find that the flow rate $Q \sim (|\Delta p|)^4$, which is consistent as found in [14, 13, 15]). These flow rate scaling are similar to what is observed by Garg and Prasad [12] in the absence of slips. We observe the back flow due to deformability in the channel when the yield surface is between $H_o/2 < H_p < (H_o + \delta)/2$, where $\delta$ is the increase in channel's height due to the elastic walls. We also observe that the deformability in the channel decreases the relative yield surface height with respect to the channel in comparison to the rigid-wall channel due to that the flow rate increases. Although wall-slip does not affect the yield surface/ plug height. It is known that due to the presence of yield stress, a threshold inlet pressure is required for the onset of flow in the channels unlike in the case of the Newtonian or power–law fluids. Garg and Prasad [12] found that below this threshold, the flow is choked in the channels with plug height the same as the channel height, that is, $H_p = \pm H/2$, we find the same observations in the presence of slips. We also find that increasing yield stress leads to decreases in the velocity in the plug flow as well as in the non–plug flow regions. Increasing yield stress also leads to increasing the yield surface height and the solid plug in the central region due to decreasing the flow rate. This is also the same in the absence of the wall-slip as observed by Garg and Prasad [12]. Further, the shear thinning index does not affect the plug height, although as the index increases the flow rate starts to decrease due to corresponding more shear thickening of the material, which is also the same in the absence of the wall-slip as observed by Garg and Prasad [12].

# References


[1] N Singla, P Verma, G Ghoshal, and S Basu. Steady state and time dependent rheological behaviour of mayonnaise (egg and eggless). *International Food Research Journal*, 20(4):2009, 2013.

[2] Qixin Zhong and Christopher R Daubert. Food rheology. In *Handbook of farm, dairy and food machinery engineering*, pages 403–426. Elsevier, 2013.

[3] GHR Kefayati and RR Huilgol. Lattice boltzmann method for the simulation of the steady flow of a bingham fluid in a pipe of square cross-section. *European Journal of Mechanics-B/Fluids*, 65:412–422, 2017.

[4] Pamela Anne Cole. *Cleaning of toothpaste from process equipment by fluid flow at laboratory and pilot scales*. PhD thesis, University of Birmingham, 2013.

[5] Anne-Laure Vayssade. *Flows of Herschel-Bulkley fluids in confined environments: applications to the cementing of oil wells*. PhD thesis, Université Pierre et Marie Curie-Paris VI, 2015.

[6] Samira Baba Hamed. Optimizing the transport of cuttings with ecological drilling muds: application to directional well. *Journal of the Brazilian Society of Mechanical Sciences and Engineering*, 42(12):619, 2020.

[7] Jason Maxey. Thixotropy and yield stress behavior in drilling fluids. In *AADE 2007 drilling fluids conference (AADE-07-NTCE-37)*, 2007.

[8] K Das. A mathematical model on the consistency coefficient of the herschel–bulkley flow of blood through narrow vessel. *Arabian Journal for Science and Engineering*, 36:405–413, 2011.

[9] Amit Bhatnagar and RK Shrivastav. Analysis of mhd flow of blood through a multiple stenosed artery in the presence of slip velocity. *International Journal of Innovative Research in Advanced Engineering (IJIRAE)*, 1(10): 250–257, 2014.

[10] Kuppalapalle Vajravelu, Sreedharamalle Sreenadh, Palluru Devaki, and Kerehalli Prasad. Mathematical model for a herschel-bulkley fluid flow in an elastic tube. *Open Physics*, 9(5):1357–1365, 2011.

[11] G Neeraja, PA Dinesh, K Vidya, and CSK Raju. Peripheral layer viscosity on the stenotic blood vessels for herschel-bulkley fluid model. *Informatics in Medicine Unlocked*, 9:161–165, 2017.

[12] Ashish Garg and Pranjal Prasad. Yield-stress shear thinning and shear thickening fluid flows in deformable channels. *ChemRxiv-Polymer Science DOI: 10.26434/chemrxiv-2023-jb7xw*, pages 1–19.

[13] Thomas Gervais, Jamil El-Ali, Axel Günther, and Klavs F Jensen. Flow-induced deformation of shallow microfluidic channels. *Lab on a Chip*, 6(4):500–507, 2006.

[14] Ivan C Christov, Vincent Cognet, Tanmay C Shidhore, and Howard A Stone. Flow rate–pressure drop relation for deformable shallow microfluidic channels. *Journal of Fluid Mechanics*, 841:267–286, 2018.

[15] Ashish Garg. Pulsatile pressure enhanced rapid water transport through flexible graphene nano/angstrom-size channels: A continuum modelling approach using the micro-structure of nanoconfined water. *ChemRxiv-Nanoscience, DOI: 10.26434/chemrxiv-2023-hlw5q*, pages 1–22.

[16] Raj P Chhabra and John Francis Richardson. *Non-Newtonian flow and applied rheology: engineering applications*. Butterworth-Heinemann, 2011.

[17] Liangyong Chen, Yufeng Duan, Changsui Zhao, and Liguo Yang. Rheological behavior and wall slip of concentrated coal water slurry in pipe flows. *Chemical Engineering and Processing: Process Intensification*, 48(7):1241–1248, 2009.

[18] Ph Coussot. Yield stress fluid flows: A review of experimental data. *Journal of Non-Newtonian Fluid Mechanics*, 211:31–49, 2014.

[19] Stylianos Varchanis, Simon J Haward, Cameron C Hopkins, Alexandros Syrakos, Amy Q Shen, Yannis Dimakopoulos, and John Tsamopoulos. Transition between solid and liquid state of yield-stress fluids under purely extensional deformations. *Proceedings of the National Academy of Sciences*, 117(23):12611–12617, 2020.

[20] Ashish Garg, Nico Bergemann, Beccy Smith, Matthias Heil, and Anne Juel. Fluidisation of yield stress fluids under vibration. *Journal of Non-Newtonian Fluid Mechanics*, 294:104595, 2021.

[21] Ashish Garg, Nico Bergemann, Beccy Smith, Matthias Heil, and Anne Juel. Fluidisation of yield stress fluids under vibration. *Science Talks*, 3:100067, 2022.

[22] Joel Koplik, Jayanth R Banavar, and Jorge F Willemsen. Molecular dynamics of fluid flow at solid surfaces. *Physics of Fluids A: Fluid Dynamics*, 1(5):781–794, 1989.

[23] Ashis Kumar Roy and Sachin Shaw. Shear augmented microvascular solute transport with a two-phase model: Application in nanoparticle assisted drug delivery. *Physics of Fluids*, 33(3), 2021.

[24] JJ Magda, M Tirrell, and HT Davis. Molecular dynamics of narrow, liquid-filled pores. *The Journal of chemical physics*, 83(4):1888–1901, 1985.

[25] Murat Barisik and Ali Beskok. Equilibrium molecular dynamics studies on nanoscale-confined fluids. *Microfluidics and Nanofluidics*, 11:269–282, 2011.

[26] M Neek-Amal, A Lohrasebi, M Mousaei, F Shayeganfar, B Radha, and FM Peeters. Fast water flow through graphene nanocapillaries: A continuum model approach involving the microscopic structure of confined water. *Applied Physics Letters*, 113(8):083101, 2018.

[27] Lucio Isa, Rut Besseling, and Wilson CK Poon. Shear zones and wall slip in the capillary flow of concentrated colloidal suspensions. *Physical Review Letters*, 98(19):198305, 2007.

[28] HJ Walls, S Brett Caines, Angelica M Sanchez, and Saad A Khan. Yield stress and wall slip phenomena in colloidal silica gels. *Journal of Rheology*, 47(4):847–868, 2003.

[29] Sridhar Kumar Kannam, BD Todd, Jesper Schmidt Hansen, and Peter J Daivis. Slip length of water on graphene: Limitations of non-equilibrium molecular dynamics simulations. *The Journal of chemical physics*, 136(2), 2012.

[30] Hamed Amini, Wonhee Lee, and Dino Di Carlo. Inertial microfluidic physics. *Lab on a Chip*, 14(15):2739–2761, 2014.

[31] Taha Sochi. Slip at fluid-solid interface. *Polymer Reviews*, 51(4):309–340, 2011.

[32] Changzheng Li, Zheng Liu, Xuyang Liu, Zhenfei Feng, and Xiaobao Mo. Combined effect of surface charge and boundary slip on pressure-driven flow and convective heat transfer in nanochannels with overlapping electric double layer. *International Journal of Heat and Mass Transfer*, 176:121353, 2021.

[33] Neil J Balmforth, Ian A Frigaard, and Guillaume Ovarlez. Yielding to stress: recent developments in viscoplastic fluid mechanics. *Annual Review of Fluid Mechanics*, 46:121–146, 2014.

[34] Francesco Picella, J-Ch Robinet, and Stefania Cherubini. On the influence of the modelling of superhydrophobic surfaces on laminar–turbulent transition. *Journal of Fluid Mechanics*, 901:A15, 2020.

[35] Peichun Amy Tsai. Slippery interfaces for drag reduction. *Journal of fluid mechanics*, 736:1–4, 2013.

[36] Keizo Watanabe, Yanuar Udagawa, and Hiroshi Udagawa. Drag reduction of newtonian fluid in a circular pipe with a highly water-repellent wall. *Journal of Fluid Mechanics*, 381:225–238, 1999.

[37] Vidit Sharma and Ashish Garg. Numerical investigation of effects of compound angle and length to diameter ratio on adiabatic film cooling effectiveness. *CoRR*, abs/1405.0560, 2014. URL `http://arxiv.org/abs/1405.0560`.

[38] Lin Qi, Ye Niu, Cody Ruck, and Yi Zhao. Mechanical-activated digital microfluidics with gradient surface wettability. *Lab on a Chip*, 19(2):223–232, 2019.

[39] Siyuan Xing, Jia Jiang, and Tingrui Pan. Interfacial microfluidic transport on micropatterned superhydrophobic textile. *Lab on a Chip*, 13(10):1937–1947, 2013.

[40] Zhifeng Zhang, Jie Xu, Bin Hong, and Xiaolin Chen. The effects of 3d channel geometry on ctc passing pressure–towards deformability-based cancer cell separation. *Lab on a Chip*, 14(14):2576–2584, 2014.

[41] Bianxiao Cui, Haim Diamant, and Binhua Lin. Screened hydrodynamic interaction in a narrow channel. *Physical review letters*, 89(18):188302, 2002.

[42] Ory Schnitzer and Ehud Yariv. Longitudinal pressure-driven flows between superhydrophobic grooved surfaces: large effective slip in the narrow-channel limit. *Physical Review Fluids*, 2(7):072101, 2017.

[43] Olubode Kolade Koriko, Kolawole S Adegbie, Nehad Ali Shah, Isaac L Animasaun, and M Adejoke Olotu. Numerical solutions of the partial differential equations for investigating the significance of partial slip due to lateral velocity and viscous dissipation: the case of blood-gold carreau nanofluid and dusty fluid. *Numerical methods for partial differential equations*, 2021.

[44] Debapriya Pinaki Mohanty, Anirudh Udupa, Anil Chandra AR, Koushik Viswanathan, James B Mann, Kevin P Trumble, and Srinivasan Chandrasekar. Mechanical behavior and high formability of palm leaf materials. *Advanced Energy and Sustainability Research*, 2(4):2000080, 2021.

[45] Paolo Bettotti and Marina Scarpa. Nanocellulose and its interface: On the road to the design of emerging materials. *Advanced Materials Interfaces*, 9(4):2101593, 2022.

[46] Ajit Behera and Ajit Behera. Advanced plastic materials. *Advanced Materials: An Introduction to Modern Materials Science*, pages 469–506, 2022.

[47] Themistoklis Karkantonis, Anvesh Gaddam, Tian Long See, Suhas S Joshi, and Stefan Dimov. Femtosecond laser-induced sub-micron and multi-scale topographies for durable lubricant impregnated surfaces for food packaging applications. *Surface and Coatings Technology*, 399:126166, 2020.

[48] Mohammad Ahmadzadehtalatapeh and Majid Mousavi. A review on the drag reduction methods of the ship hulls for improving the hydrodynamic performance. *International Journal of Maritime Technology*, 4:51–64, 2015.

[49] Teodor Akinfiev, Alexander Janushevskis, and Egons Lavendelis. A brief survey of ship hull cleaning devices. *Transport & Engineering*, 24(7), 2007.

[50] Changhui Song and Weicheng Cui. Review of underwater ship hull cleaning technologies. *Journal of marine science and application*, 19(3):415–429, 2020.

[51] Cunming Yu, Mengfei Liu, Chunhui Zhang, Hao Yan, Minghui Zhang, Qingshan Wu, Mingjie Liu, and Lei Jiang. Bio-inspired drag reduction: From nature organisms to artificial functional surfaces. *Giant*, 2:100017, 2020.

[52] Seung Joong Kim, Hae Nyeok Kim, Sang Joon Lee, and Hyung Jin Sung. A lubricant-infused slip surface for drag reduction. *Physics of Fluids*, 32(9), 2020.

[53] Susheel Kumar, Krishna Murari Pandey, and Kaushal Kumar Sharma. Advances in drag-reduction methods related with boundary layer control–a review. *Materials Today: Proceedings*, 45:6694–6701, 2021.

[54] Santosh Kumar, Fei Ye, Sergey Dobretsov, and Joydeep Dutta. Nanocoating is a new way for biofouling prevention. *Frontiers in Nanotechnology*, 3:771098, 2021.

[55] B Quan Luna, A Remaître, Th WJ Van Asch, J-P Malet, and CJ Van Westen. Analysis of debris flow behavior with a one dimensional run-out model incorporating entrainment. *Engineering geology*, 128:63–75, 2012.

[56] Daniel Bonn, Morton M Denn, Ludovic Berthier, Thibaut Divoux, and Sébastien Manneville. Yield stress materials in soft condensed matter. *Reviews of Modern Physics*, 89(3):035005, 2017.

[57] Ashish Garg. Fluidisation of yield stress materials under vibration. *PhD thesis, The University of Manchester*, pages 1–175, 2022.

[58] Robert J Daniello, Nicholas E Waterhouse, and Jonathan P Rothstein. Drag reduction in turbulent flows over superhydrophobic surfaces. *Physics of Fluids*, 21(8), 2009.

[59] Hyungmin Park, Chang-Hwan Choi, and Chang-Jin Kim. Superhydrophobic drag reduction in turbulent flows: A critical review. *Experiments in Fluids*, 62:1–29, 2021.

[60] NS Deshpande and M Barigou. Vibrational flow of non-newtonian fluids. *Chemical Engineering Science*, 56(12): 3845–3853, 2001.

[61] John J McKetta. *Encyclopedia of Chemical Processing and Design: Volume 37-Pipeline Flow: Basics to Piping Design*. Routledge, 2022.

[62] Chi H Lee, Venkat Moturi, and Yugyung Lee. Thixotropic property in pharmaceutical formulations. *Journal of controlled release*, 136(2):88–98, 2009.

[63] Christopher Marriott. Viscosity, rheology and the flow of fluids. *Aulton's Pharmaceutics E-Book: The Design and Manufacture of Medicines*, page 94, 2013.

[64] Ozge Inal, Gulin Amasya, Zerrin Sezgin Bayindir, and Nilufer Yuksel. Development and quality assessment of glutathione tripeptide loaded niosome containing carbopol emulgels as nanocosmeceutical formulations. *International Journal of Biological Macromolecules*, 241:124651, 2023.

[65] Dhruv Mehta, Adithya Krishnan Thota Radhakrishnan, Jules Van Lier, and Francois Clemens. A wall boundary condition for the simulation of a turbulent non-newtonian domestic slurry in pipes. *Water*, 10(2):124, 2018.

[66] Ali Faghani, Samya Sen, Mahdi Vaezi, and Amit Kumar. Rheology of fibre suspension flows in the pipeline hydro-transport of biomass feedstock. *Biosystems Engineering*, 200:284–297, 2020.

[67] Weiqi Fu, Zhiyuan Wang, Baojiang Sun, Jianchun Xu, Litao Chen, and Xuerui Wang. Rheological properties of methane hydrate slurry in the presence of xanthan gum. *SPE Journal*, 25(05):2341–2352, 2020.

[68] Prashanta Kumar Mandal. An unsteady analysis of non-newtonian blood flow through tapered arteries with a stenosis. *International journal of non-linear mechanics*, 40(1):151–164, 2005.

[69] S Sreedharamalle, D Palluru, and D Reddy. Krishnaiah. unsteady flow of a jeffrey fluid in an elastic tube with a stenosis. In *Proceedings of the International Conference on Fluid Dynamics and Thermodynamics Technologies*, volume 33, page 1, 2012.

[70] Praveen Chandrashekar and Ashish Garg. Vertex-centroid finite volume scheme on tetrahedral grids for conservation laws. *Computers & Mathematics with Applications*, 65(1):58–74, 2013.

[71] Shivam Singhal, Yayati Gupta, and Ashish Garg. Fluid dynamics android application: An efficient semi-implicit solver for compressible flows. *Preprints - DOI: 10.20944/preprints201910.0309.v1*, pages 1–24, 2019.

[72] ACL Barnard, WA Hunt, WP Timlake, and E Varley. A theory of fluid flow in compliant tubes. *Biophysical journal*, 6(6):717–724, 1966.

[73] Mette S Olufsen. A one-dimensional fluid dynamic model of the systemic arteries. In *Computational Modeling in Biological Fluid Dynamics*, pages 167–187. Springer, 2001.

[74] NP Smith, AJ Pullan, and Peter J Hunter. An anatomically based model of transient coronary blood flow in the heart. *SIAM Journal on Applied mathematics*, 62(3):990–1018, 2002.

[75] SJ Sherwin, V Franke, J Peiró, and K20389821200 Parker. One-dimensional modelling of a vascular network in space-time variables. *Journal of engineering mathematics*, 47:217–250, 2003.

[76] Taha Sochi. The flow of newtonian and power law fluids in elastic tubes. *International Journal of Non-Linear Mechanics*, 67:245–250, 2014.

[77] Lorenzo Fusi, Angiolo Farina, Fabio Rosso, and Sabrina Roscani. Pressure driven lubrication flow of a bingham fluid in a channel: A novel approach. *Journal of Non-Newtonian fluid mechanics*, 221:66–75, 2015.

[78] Pandelitsa Panaseti, Yiolanda Damianou, Georgios C Georgiou, and Kostas D Housiadas. Pressure-driven flow of a herschel-bulkley fluid with pressure-dependent rheological parameters. *Physics of fluids*, 30(3), 2018.

[79] Lorenzo Fusi and Angiolo Farina. Peristaltic axisymmetric flow of a bingham fluid. *Applied Mathematics and Computation*, 320:1–15, 2018.

[80] Kostas D Housiadas, Iasonas Ioannou, and Georgios C Georgiou. Lubrication solution of the axisymmetric poiseuille flow of a bingham fluid with pressure-dependent rheological parameters. *Journal of Non-Newtonian Fluid Mechanics*, 260:76–86, 2018.

[81] Lorenzo Fusi, Kostas D Housiadas, and Georgios C Georgiou. Flow of a bingham fluid in a pipe of variable radius. *Journal of Non-Newtonian Fluid Mechanics*, 285:104393, 2020.

[82] CLMH Navier. Mémoire sur les lois du mouvement des fluides. *Mémoires de l'Académie Royale des Sciences de l'Institut de France*, 6(1823):389–440, 1823.

[83] Miccal T. Matthews and James M. Hill. Nano boundary layer equation with nonlinear navier boundary condition. *Journal of Mathematical Analysis and Applications*, 333(1):381 – 400, 2007. ISSN 0022-247X. doi: https://doi.org/10.1016/j.jmaa.2006.08.047.

[84] Jaroslav Hron, C Le Roux, Josef Málek, and KR Rajagopal. Flows of incompressible fluids subject to navier's slip on the boundary. *Computers & Mathematics with Applications*, 56(8):2128–2143, 2008.

[85] Charles Edward Fisher. The effects of a navier-slip boundary condition on the flow of two immiscible fluids in a microchannel. 2013.

[86] Peter H Mott, John R Dorgan, and CM Roland. The bulk modulus and poisson's ratio of "incompressible" materials. *Journal of Sound and Vibration*, 312(4-5):572–575, 2008.

[87] Ashish Garg. Aerodynamics. In *GATE Aerospace Forum Educational Services*, 2015.

[88] Frank M White. *Fluid mechanics.* New York, 1990.

[89] George Keith Batchelor. *An introduction to fluid dynamics.* Cambridge university press, 1967.

[90] Brian J Kirby. *Micro-and nanoscale fluid mechanics: transport in microfluidic devices.* Cambridge university press, 2010.